

Statistical comparison of TEC derived from GPS and ISR observations at high latitudes

Roman A. Makarevich¹ and Michael J. Nicolls²

Received 31 January 2013; revised 11 July 2013; accepted 25 July 2013; published 15 August 2013.

[1] A comprehensive data set collected with the Poker Flat Incoherent Scatter Radar (PFISR) and GPS receiver in Fairbanks, Alaska (magnetic latitude = 65.4°N) in 2007–2010 is employed to analyze and compare the total electron content (TEC) estimates derived from two radio techniques at high latitudes. The average TEC trends are shown to be largely similar and consistent with expectations based on solar conditions. The TEC residuals expressed as the difference and ratio between the PFISR- and GPS-derived TEC are evaluated to be below 2 total electron content units ($\text{TECU} = 10^{16} \text{ electrons m}^{-2}$) and 0.7–0.8, respectively, with some dependence on solar conditions. The agreement between TEC estimates is examined by limiting the difference between the GPS satellite and PFISR beam elevations to 2.5° and postintegrating GPS measurements over the period of each PFISR measurement. Factors controlling the agreement are investigated, including possible roles of GPS satellite bias, GPS elevation angle, and topside contribution to TEC. It is demonstrated that the best agreement, expressed as a linear correlation and a fraction of points consistent with the linear trend, is achieved with satellites at the largest elevation angles and smallest distances from PFISR, which are a possible effect of small spatial differences and unremoved differential biases. Estimates of the topside contribution to TEC range between 14% and 30% and are most consistent during daytime hours, while observations near the solar terminator and during the night suffer from large uncertainties.

Citation: Makarevich, R. A., and M. J. Nicolls (2013), Statistical comparison of TEC derived from GPS and ISR observations at high latitudes, *Radio Sci.*, 48, 441–452, doi:10.1002/rds.20055.

1. Introduction

[2] The total electron content (TEC) is an important characteristic of the ionization levels and processes in the near-Earth space, particularly near the ionospheric *F* region peak. As such it has been used in numerous previous studies of ionospheric dynamics and climatology, with one important focus being on responses to geomagnetic disturbances (e.g., see recent reviews by *Mendillo* [2006] and *Mendillo and Klobuchar* [2006]). In the GPS era, global observations of the vertical TEC (VTEC) have provided new insights into connections between different latitudinal domains in the coupled magnetosphere-ionosphere system such as storm-enhanced density plumes and associated convection channels extending all the way from polar to midlatitudes [*Foster et al.*, 2005].

[3] High-resolution incoherent scatter radar (ISR) observations of electron density and other parameters in the ionosphere provide a complementary way to examine the same processes but on a smaller scale. With GPS TEC observations providing a global context, ISR observations are often used to infer critical information about the vertical and small-scale ionospheric structure [e.g., *Nicolls et al.*, 2004; *Foster et al.*, 2005; *Huang et al.*, 2005].

[4] Efforts to cross-compare and calibrate ISR and GPS observations of TEC are important from both instrumental and geophysical points of view. These efforts provide additional tools that can be used to fine-tune data processing techniques and to gain new information about geophysical processes that may underlie discrepancies between two sets of observations. At low magnetic latitudes, *Makela et al.* [2000] compared Arecibo ISR observations of the electron density up to an altitude of 1500 km complemented by a numerical model of the plasmasphere with nearly collocated GPS TEC measurements for two events. They obtained an excellent agreement between time variations of the ISR- and GPS-derived line-of-sight (l-o-s) or slant TEC (STEC) estimates. At high latitudes, *Lilensten and Cander* [2003] used the electron densities at 90–498 km from the main dish of the European Incoherent Scatter (EISCAT) radar system in Tromsø, Norway, to derive an estimate of the TEC (called Integrated TEC or ITEC₄₉₈ in that study). *Lilensten and Cander* [2003] compared the ITEC₄₉₈ estimates with the

¹Geophysical Institute and Department of Physics, University of Alaska Fairbanks, Fairbanks, Alaska, USA.

²Center for Geospace Studies, SRI International, Menlo Park, California, USA.

Corresponding author: R. A. Makarevich, Geophysical Institute and Department of Physics, University of Alaska Fairbanks, 903 Koyukuk Drive PO Box 757320, Fairbanks, AK 99775-7320, USA. (r.makarevich@gi.alaska.edu)

TEC values from two collocated GPS receivers for six events and found a good agreement overall, but also a few cases of $\text{ITEC}_{498} > \text{TEC}$, which was interpreted through contribution from the protonosphere [e.g., *Lunt et al.*, 1999].

[5] Other examples of geophysical processes that can potentially affect the agreement between ISR and GPS observations include weaker F region during the night and denser plasmasphere under storm and solar maximum conditions; both result in a greater plasmaspheric contribution to TEC [*Belehaki et al.*, 2003; *Yizengaw et al.*, 2008]. The plasmasphere is unlikely to contribute significantly to TEC measured at magnetic latitude (MLAT) $> 60^\circ$ [e.g., see *Yizengaw et al.*, 2008 and their Figure 1], but some topside contribution is expected. Calculating the residual values between ITEC and TEC measurements (expressed as a simple difference $\text{TEC} - \text{ITEC}$, their ratio $r = \text{ITEC}/\text{TEC}$, or fractional difference $1 - r$) allows this contribution to be estimated. The observational efforts in this area have included mostly work at midlatitudes and low latitudes using GPS and vertical sounders [e.g., *Belehaki et al.*, 2003; *Meza et al.*, 2008], while similar efforts based on extended density profiles from ISR measurements at high latitudes focused on analysis of individual events [*Lilensten and Cander*, 2003; *Lilensten et al.*, 2005], mostly due to limited ISR data availability.

[6] The first motivation for this work is the need to further understand and quantify the limitations of ISR and GPS techniques, in particular those limitations associated with the limited altitude range of ISR measurements and with the significant effects exerted on GPS TEC estimates by differential instrument biases (DIBs). The second motivation is the need to quantify the plasma content in the topside ionosphere and plasmasphere; complementary ISR and GPS measurements offer additional opportunities to do so because their data sets are extensive.

[7] The recent deployment of a new generation of ISR systems based on an Advanced Modular ISR (AMISR) design capable of providing good-quality data with nearly continuous temporal coverage when using a low-duty cycle [*Sojka et al.*, 2009] has created new opportunities to address both of these issues, particularly in the auroral region, using the AMISR system at Poker Flat, Alaska or PFISR.

[8] Figure 1a illustrates these opportunities by showing the approximate extent of coverage by various ISR systems in the Northern Hemisphere. The yellow lines represent the approximate viewing areas of ISRs up to an altitude of 400 km. The oval-shaped outlines correspond to (from left to right) the EISCAT dishes at Svalbard and Tromsø and the ISRs at Søndrestrøm and Millstone Hill. The star-shaped outlines show the PFISR as well as the north and south faces of an AMISR system at Resolute Bay, Canada (RISR-N and RISR-C). The green lines are the lines of equal magnetic latitudes of 60°N and 70°N given by the Polar Anglo-American Conjugate Experiment (PACE) model [*Baker and Wing*, 1989]. Figure 1a shows that PFISR is particularly well-suited for statistical comparisons with GPS at high latitudes due to its location within the auroral region.

[9] The reference height of 350 km was used in all data analyses and comparisons throughout the entire study as further described in section 2. The blue lines near PFISR in Figure 1a thus show the locations of the sub-ionospheric points at 350 km as seen from Poker Flat (PF)

(point on a l-o-s between PF and the GPS satellite location at an altitude of 20,200 km). GPS satellites do not pass directly over the high-latitude region, as illustrated by the red surface tracks in Figure 1a. Therefore, there is an oval-shaped “blind spot” around the PF location (Figure 1a). Nevertheless, an extended area of possible conjunctions exists in the equatorial portion of the PFISR field-of-view (FoV).

[10] This is further illustrated in Figure 1b, which shows the area near PF with actual conjunctions on 1 May 2008. The pink lines show the three selected beams of PFISR to a height of 350 km (not to scale), and the colored dots on blue lines represent GPS satellite locations with elevation angles above 75° . The location of GPS receiver in Fairbanks, Alaska (IGS station FAIR) is also shown; the great-circle distance between PF and FAIR at a 350 km altitude is only 18 km. Considering that (1) the elevation angle of the field-aligned PFISR beam (equatorward directed beam in Figure 1b) is 77.5° , (2) the resulting distances between GPS sub-ionospheric points and PFISR beam at 350 km are very small (10–80 km), and (3) an extensive data set of electron densities has been accumulated by PFISR in the first few years of its operations, this configuration presents an excellent opportunity to analyze and directly compare the GPS- and PFISR-derived TEC estimates with minimal uncertainties due to spatial variations and with minimal data postprocessing.

[11] The main aim of the current study is to investigate the factors that affect agreement between the two techniques by statistically analyzing the extensive data set of TEC estimates from GPS and PFISR observations. The specific objectives are as follows: (1) to analyze the average behavior of GPS- and PFISR-derived TEC, focusing on their solar cycle, seasonal, and diurnal trends, (2) to investigate the topside ionosphere contribution to TEC at auroral latitudes by analyzing TEC residuals obtained from the two techniques, and (3) to quantify the agreement between TEC estimates using close GPS-PFISR conjunctions and elucidate the factors that control how closely the estimates agree.

2. Data Selection and Processing

[12] The ISR data set employed in this study comprised data from the PFISR system located at the Poker Flat Research Range (65.13°N , 147.47°W , MLAT = 65.4°N) near Fairbanks, Alaska [*Heinselmann and Nicolls*, 2008; *Sojka et al.*, 2009]. PFISR is a phased-array system with a beam that can be steered electronically in many directions within the viewing area (Figure 1). Data from multiple beams can be collected nearly simultaneously (sequentially on a pulse-by-pulse basis but with a very high time cadence) within the same integration period. PFISR has been in routine operation since 1 March 2007, and the current study considered data collected from 1 March 2007 to 31 December 2010. In this study, we employed only the data collected in the International Polar Year (IPY) series of modes [*Sojka et al.*, 2009]. In the low-duty-cycle IPY modes, PFISR observed either along a single, field-aligned beam 64157 (IPY01 mode: azimuth 154.3° east of geographic north and elevation 77.5°), along three beams (IPY02, IPY04: beams 64157, 64964, and 65066 shown in Figure 1b), or along four

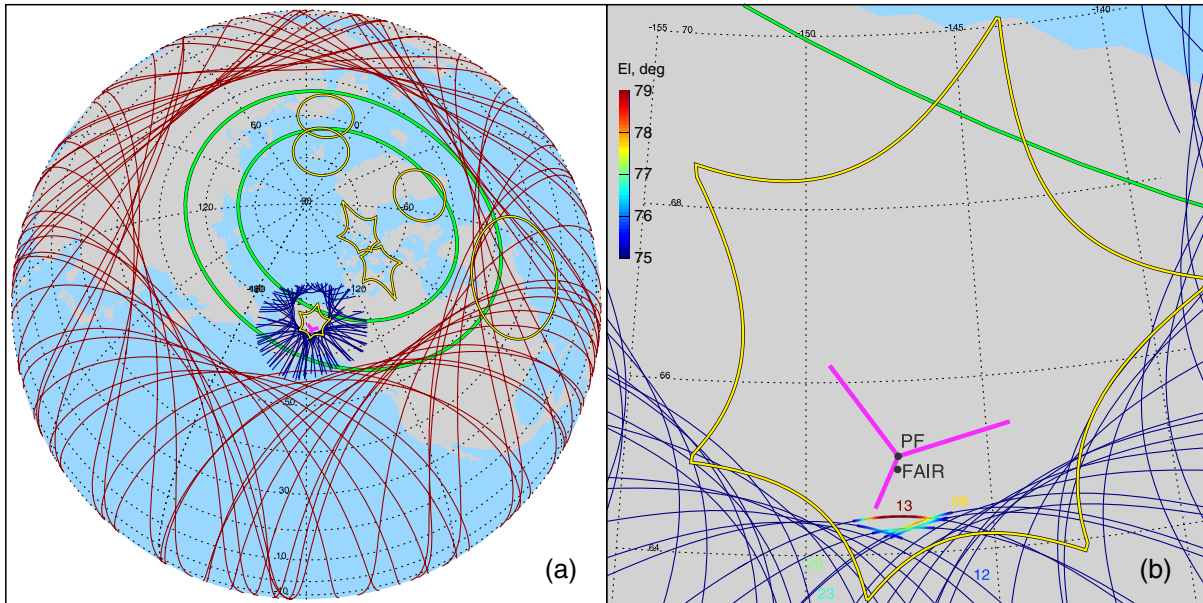


Figure 1. (a) Map of the high northern latitudes showing field-of-view outlines of various ISR systems at 400 km (yellow) and an example of GPS surface tracks on 1 May 2008 (red). The thick green lines are the lines of equal magnetic latitudes of 60°N and 70°N. The pink straight lines are the three beams of an ISR system in Poker Flat, Alaska (PFISR) up to an altitude of 350 km. The blue lines near PFISR are the GPS sub-ionospheric points at 350 km on 1 May 2008 as seen from the GPS receiver in Fairbanks, Alaska (GPS station code: FAIR). (b) The close-up near PFISR also shows PFISR and FAIR locations. The locations on GPS tracks with satellite elevation angles above 75° are color coded as given by the color bar in Figure 1b. The GPS satellite numbers (PRN) are also shown nearby, color coded in maximum elevation angle.

beams (IPY05, IPY15, and IPY17: three beams as before plus vertical beam 64016).

[13] The IPY mode uses two sets of interleaved pulses: a long pulse (LP) with 72 km range resolution used for *F* region studies and an alternating code (AC) pulse with 4.5 km resolution used for *E* region studies. The data products are also computed every half-pulse width or every 36 km for LP measurements and 2.25 km for AC measurements. The data integration period is ~ 15 min. The electron density is obtained from the calibrated power using LP plasma line observations over the same observational period. Only the LP electron density data were employed in the current study. The accuracy for these data is estimated to be within 5% after calibration [Sojka *et al.*, 2009]. For further details on technical specifications of the PFISR system and IPY modes, the reader is referred to Heinselmann and Nicolls [2008] and Sojka *et al.* [2009].

[14] All the PFISR IPY data collected from 1 March 2007 to 31 December 2010 were considered in the current study, except for data from several days in 2008–2010 that were excluded because of poor data quality. This was determined by examining all the daily density plots (similar to Figure 2 of Sojka *et al.* [2009]) and rejecting days with noisy data. The excluded days in the YYYYMMDD format were the following: 20080114, 20080507, 20080615, 20090830, 20090831, 20091004, 20091201, 20100103, 20100604, and 20100916.

[15] In addition, electron densities that exceeded $2.2 \times 10^{11} \text{ m}^{-3}$ were also excluded. Spuriously high density values may represent coherent returns, satellite echoes,

or naturally enhanced ion-acoustic lines (NEIALs) (e.g., review by Sedgemore-Schulthess and St. Maurice [2001]) which are unsuitable for TEC estimates. The occurrence frequency of enhanced ISR returns near solar cycle minimum is ~ 100 data dumps per 1 million at 10 s resolution [Rietveld *et al.*, 1996]. In the worst-case scenario that assumes that the entire 15 min data integration period will be contaminated by a single return, there is a 0.9% chance that any PFISR measurement is affected by enhanced returns. The top 1% of all densities collected during year 2008 start at $2.2 \times 10^{11} \text{ m}^{-3}$; this value was selected as the maximum density in our data set to limit the potential impact of enhanced ISR returns on ISR-derived electron content estimates.

[16] The IPY modes with usable LP data were run for $\sim 59\%$, 56%, 59%, and 58% of the time in 2007, 2008, 2009, and 2010, respectively. The seasonal coverage was fairly uniform (except for 2007 operations that started in March), and the Magnetic Local Time (MLT) coverage was slightly biased toward daytime ($\sim 70\%$ versus $\sim 45\%$ during the night) with significantly lower coverage at 21:00–23:00 UT ($\sim 10:00$ – $12:00$ MLT) in 2008 ($\sim 15\%$) because a special mode was run for most of 2008 during that 2 h period. Since the daytime observations were otherwise well represented in the data set and since there was no such gap in other yearly data sets, all 4 years were considered in the current study.

[17] For each data integration period, the electron density data were further integrated over the range of the LP data (102–678 km) to produce a STEC estimate in total electron content units (TECU, 1 TECU = 10^{16} electrons m^{-2}) along each PFISR beam. The PFISR-derived STEC estimates thus

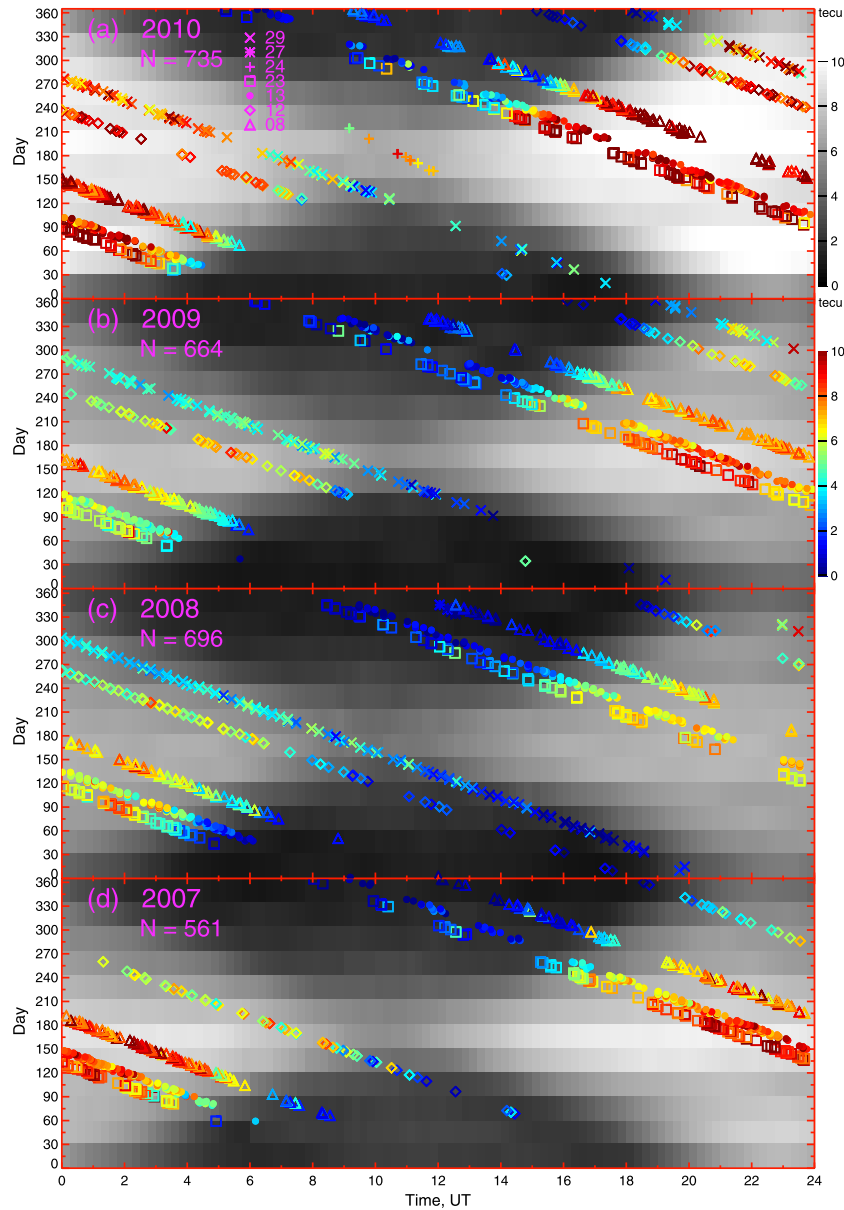


Figure 2. GPS and PFISR conjunctions versus universal time and day of the year. Each panel (a)-(d) represents 1 year of data as indicated in the top-left corner. Each symbol represents one conjunction point color coded in TEC derived from PFISR and symbol coded in PRN. The total number of conjunctions N for each year is also given. The gray-scale background represents the GPS TEC in 1 month and 15 min bins. The TEC scales are indicated to the right of Figures 2a and 2b, while the symbol-coding scheme is shown in Figure 2a.

refer to the bulk of the ionosphere but do not include a possible contribution from the topside ionosphere and plasmasphere, although the latter contribution is expected to be small at these latitudes, as discussed in section 1. The PFISR values were also corrected to produce the VTEC estimates in the same way as the GPS-derived STEC values were, as described below. For beam 64157, this correction translates to the 100–663 km height range and a mapping factor $M = 0.9787$ ($VTEC = M \cdot STEC$). Throughout the rest of this paper, the VTEC estimates obtained from PFISR will be referred to as the ITEC. The standard uncertainty estimates for the electron density were propagated through the range

integration algorithm to yield the uncertainty estimate for ITEC. Since PFISR beam direction was fixed, no additional uncertainty due to mapping was introduced.

[18] In this study, we also employed the GPS phase and pseudorange delay data at 30 s time resolution; these data were processed to give VTEC estimates. The phase-based delays were leveled with the pseudorange delays for each phase-connected arc of data [Mannucci *et al.*, 1998], limiting elevations to angles above 10° . The DIB estimates for all GPS satellites and for the FAIR station were taken as auxiliary data products of the Global Ionospheric Mapping (GIM) technique by the NASA Jet Propulsion Laboratory (JPL)

[Mannucci *et al.*, 1998] and removed from the data. The locations of sub-ionospheric points and the VTEC values were computed using a Single Layer Model for the reference ellipsoid WGS-84 at an altitude of 350 km. The altitude of 350 km was selected as a compromise between the typical 250–300 km altitude of peak density observed by PFISR and the 450 km altitude used in JPL GIM.

[19] For each individual GPS satellite-receiver pair, the absolute STEC estimate accuracy is set by random errors in pseudorange delay data. Together with DIBs, these random errors determine the absolute VTEC estimate uncertainty based on global mapping techniques. The precision in DIBs from JPL GIM is below 1 TECU at midlatitudes during quiet times and below 2 TECU at low latitudes [Komjathy *et al.*, 2005]. For the current study involving local comparisons using single-receiver GPS measurements, a typical root-mean-square (RMS) error in DIBs was quite small, < 0.1 TECU, and the RMS errors after post-integration at ~ 15 min intervals were the major source of uncertainty in individual VTEC estimates. All points with large uncertainties (> 2 TECU in either VTEC or ITEC; $\sim 25\%$ of all points) were rejected from further analysis. A further restriction (relative errors $< 50\%$) was introduced for data sets with large statistics employed in sections 3 and 4 where we also computed RMS errors for each binning analysis.

[20] For comparisons with PFISR, all GPS-PFISR conjunctions were found from the navigation data. A conjunction was defined to be all GPS data points within a 15 min PFISR data integration period and with GPS satellite elevation angles ϵ exceeding 75° . Figure 1b shows these conjunctions as dots color coded to represent GPS elevation angle ϵ on blue tracks. The GPS satellite identifiers as pseudo-random noise (PRN) numbers, or simply PRNs, are also shown nearby. Figure 1b shows that, for the day shown, five GPS satellites had conjunctions with PFISR, with PRNs 12, 23, 29, 08, and 13 corresponding to progressively larger angles ϵ . This result was typical of year 2008. In other years a few other PRNs contributed to the data set but only at ϵ near 75° , so that the largest angles ϵ (and better conjunctions) were always with PRNs 08 and 13. Importantly, the GPS VTEC data were matched in time with those from PFISR; i.e., they were averaged over each ~ 15 min PFISR time integration period. Moreover, since GPS elevations did not exceed 80° , the nominal distance between the GPS and PFISR measurement locations was relatively small, ranging between 10 and 80 km.

[21] Despite these relatively small nominal distances, different GPS satellites referred to slightly different ranges of elevation angle ϵ ; for example, PRN 13 always had $\epsilon > 78^\circ$, while PRN 23 had $\epsilon = 76.5^\circ - 77.0^\circ$. This introduces a small but systematic difference between STEC estimates due to differently inclined paths through the ionosphere. In order to consider all available PRNs in the same analysis, STEC were converted into VTEC as described above. In addition, VTEC estimates are routinely obtained as a final product of GPS data analysis and in this sense the STEC-to-VTEC conversion facilitates comparisons with other studies.

[22] The GPS satellites orbit in such a way that a given location is covered during a progressively earlier time period as the day of the year increases, and hence different universal time (UT) intervals and seasons were not sampled

equally (in our selection of good conjunctions). This is illustrated in Figure 2 which shows the coverage of different UT and monthly intervals by our matched GPS-PFISR data. The symbols represent conjunctions, symbol coded in PRN and color coded in ITEC values. The respective coding schemes are shown in Figures 2a and 2b. The gray-scale background represents the VTEC values from GPS observations (without matching to PFISR) binned in monthly and 15 min intervals.

[23] Figure 2 shows a characteristic TEC pattern associated with diurnal and seasonal variations in both color coding and background gray scale. Solar cycle effects are also evident in both data sets. There is more saturation (at 10 TECU) observed in GPS observations in 2010 during summer and near noon (magnetic midnight is $\sim 11:00$ UT), as compared to ITEC values; this result is expected given a narrower PFISR height range. A detailed analysis of these differences or TEC residuals is presented later in sections 3–5. The overall agreement in TEC trends is reasonable.

[24] On average, ~ 700 conjunctions occurred every year (after exclusion of large-error points) except for in 2007, and most areas of the graph were sampled well. A smaller number of conjunctions in 2007 occurred because PFISR observations did not begin until March and some navigation data for PRN 29 were missing. In 2008–2010, the largest gap was observed between PRNs 29 and 23 (crosses and squares in Figure 2). This unequal sampling of some UT and monthly periods presents challenges for analysis of diurnal and seasonal trends without some further grouping (e.g., combining all summer months together). Nevertheless, the conjunctions refer to a wide variety of solar zenith angle (SZA) conditions, which allows for a number of direct comparisons (section 5). In addition, the average trends of selected parameters can be analyzed and compared without such a strict matching (section 3).

3. Comparison of Average Trends in the TEC Data

[25] In this section, the average trends in GPS VTEC and PFISR ITEC and their residuals are analyzed and compared. The first row of Figure 3 shows the VTEC data averaged for each monthly and hourly interval for quiet-time periods ($Kp < 3$). The format of each panel is the same; UT is shown on the x axis, and month is shown on the y axis. The columns refer to years from 2007 to 2010. Similarly, the other three rows show the average PFISR ITEC, the residual VTEC–ITEC, and the ratio ITEC/VTEC, respectively. The color scales are shown to the right.

[26] Similar to gray-scale background in Figure 2, each panel in the first two rows of Figure 3 clearly shows diurnal and seasonal variations, while solar cycle effects are evident from comparing different columns. The elevated TEC clearly corresponds to daytime observations, while nighttime TEC is smaller, as expected. White cells in the second row correspond to nighttime periods when other, non-IPY modes were predominantly run by PFISR (e.g., near 22:00 UT in 2008) or when most PFISR data were rejected because of large errors.

[27] The average TEC residuals in the third row show a somewhat different pattern. Similar to TEC, the daytime

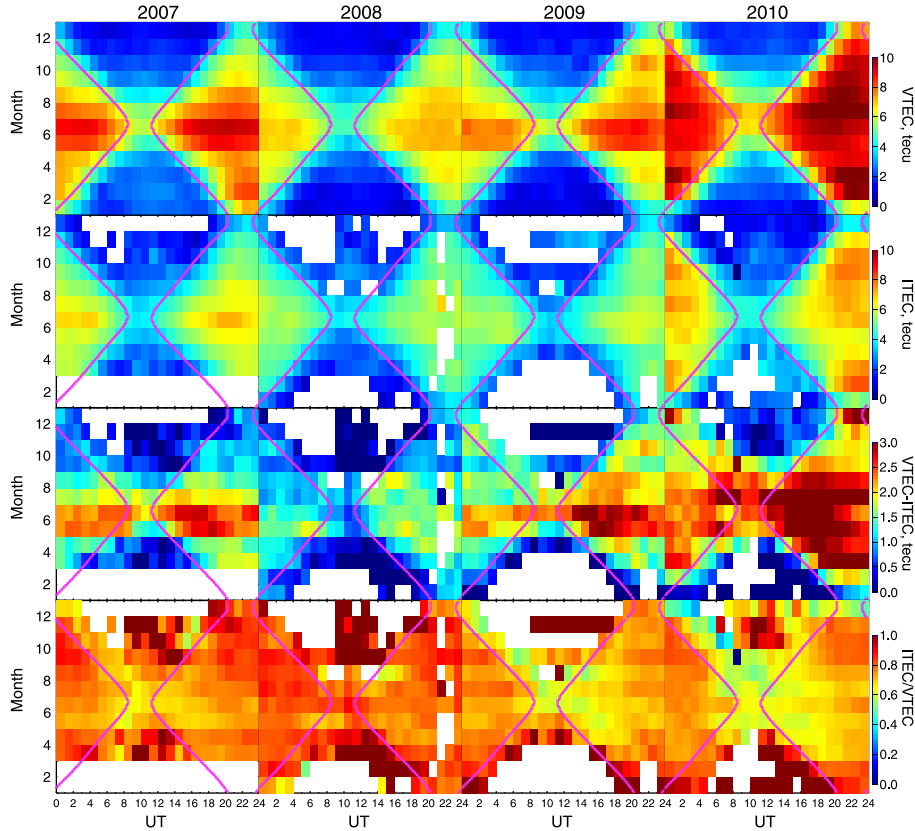


Figure 3. Seasonal, diurnal, and solar cycle trends in the quiet-time ($Kp < 3$) GPS VTEC (top row) and PFISR ITEC (second row). Also shown are the average difference $VTEC - ITEC$ (third row) and the average ratio $ITEC/VTEC$ (bottom row). Each column represents 1 year of data as shown at the top of each column. The surface sunset and sunrise times are shown by the pink lines.

TEC residual values were generally higher than those at nighttime, but the maximum positions in UT and the UT dependence itself were much less consistent between subsequent months; the pattern is not as smooth as for TEC. Nevertheless, all three effects (diurnal, seasonal, and solar cycle) are present. One should note here that the above-described trends and features refer to relatively small values (0–4 TECU) which were often within standard deviations (1–2 TECU; not shown here for brevity), but the general similarity between different years and months suggests that these trends are real. A related analysis with explicit consideration of uncertainties is also presented in section 4. Finally, the bottom row of Figure 3 shows that the average $ITEC/VTEC$ ratio ranged between 0.6 and 1.2 and also exhibited all three effects. The pattern is generally the inverse of that observed for the residual expressed as a difference, except that here we also observe a consistent decrease just after sunset lasting 2–3 h in July–December which was not obvious from the third-row panels.

[28] The TEC residuals can be attributed to the topside contribution to TEC as discussed in section 1, and the above analysis indicates that this contribution varies generally in line with the contribution from the bulk of the ionosphere represented by ITEC. One potentially important exception to this was a significantly higher morning (12:00–24:00 UT)

than evening (00:00–08:00 UT) maximum, particular during summer. This is further discussed in section 7.2.

4. TEC Dependence on Solar Conditions

[29] Figures 4a and 4c show the ITEC versus SZA (χ) and Figures 4b and 4d show the VTEC versus SZA (χ). The data are color coded in point occurrence in Figures 4a and 4b and in mean 0.1–50 nm Solar Heliospheric Observatory (SOHO) EUV flux in Figures 4c and 4d. Figures 4a and 4b also show TEC values binned in intervals of $\chi = 5^\circ$ with associated standard deviations. The two selected fitted trends at $\chi < 90^\circ$ are also given. The fit function expressions are shown in the bottom left of Figures 4a and 4b, along with the goodness-of-fit chi-squared parameter. The two groups of binned values and trends in Figures 4c and 4d are for high (red) and low (blue) EUV flux values. The critical value of 1.78×10^{10} photons $\text{cm}^{-2} \text{s}^{-1}$ was selected to split the data set into two halves: below and above this flux value. The binned values were shifted slightly in χ when plotted in Figures 4b and 4d to avoid overlapping.

[30] Figure 4e presents the residuals $VTEC - ITEC$ and Figure 4f shows the ratio $ITEC/VTEC$ obtained from the TEC binned values shown in Figures 4a–4d. Here black points with uncertainties refer to all flux values, i.e., differences/ratios between the binned values in Figures 4a

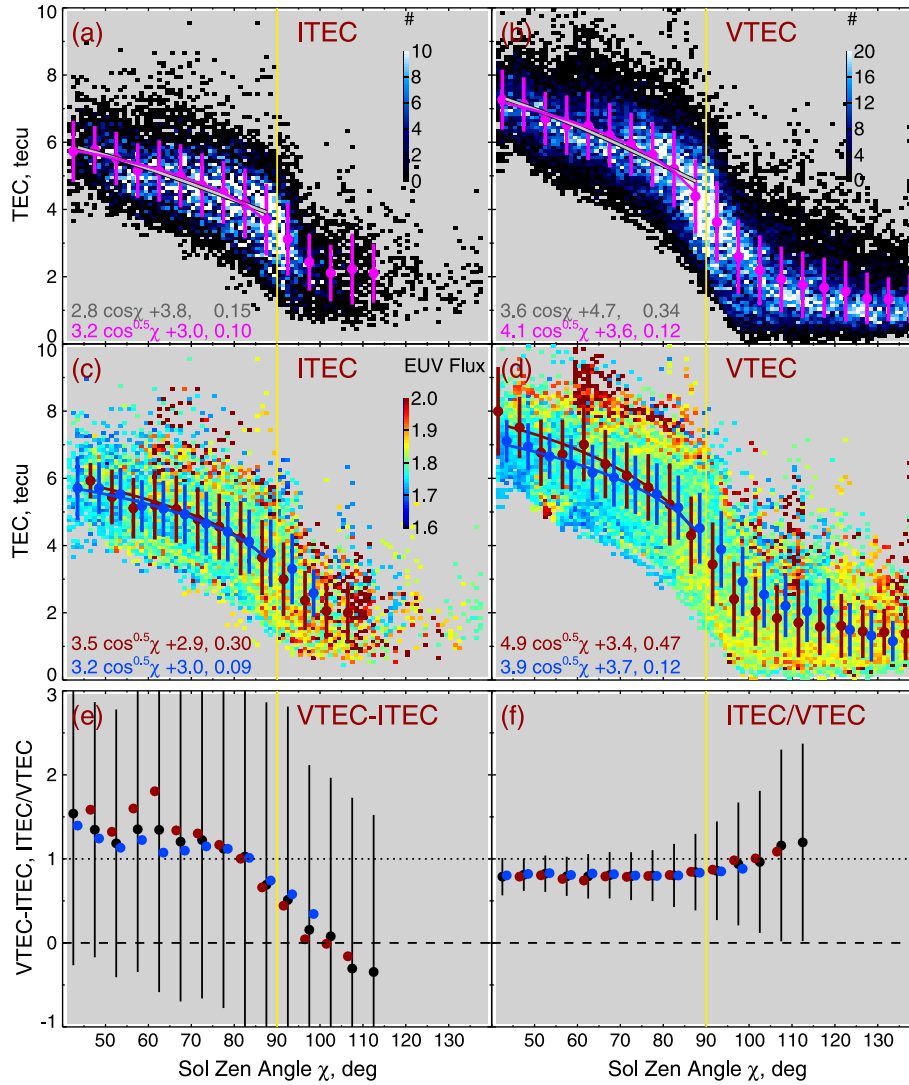


Figure 4. Two-dimensional point occurrence plots of (a) PFISR ITEC and (b) GPS VTEC versus solar zenith angle χ in 2008. (c and d) The same data but color coded in the mean SOHO EUV flux 0.1–50 nm in units of 10^{10} photons $\text{cm}^{-2} \text{s}^{-1}$. Figures 4a and 4b also show the binned values of TEC and two selected least-squares fits at $\chi < 90^\circ$. The fitted trend expressions are shown in the bottom left corner along with the chi-squared parameter. The fits in Figures 4c and 4d are for low (blue) and high (red) EUV fluxes (below or above 1.78). The bottom panels show (e) the difference between binned VTEC and ITEC values and (f) their ratio ITEC/VTEC for all (black), low (blue), and high (red) flux values.

and 4b, while red and blue points refer to high and low fluxes, respectively, from the binned values in Figures 4c and 4d. The uncertainties in these values were very similar to those given by the black lines and were omitted here for clarity.

[31] Figure 4 shows that TEC changes drastically as the sun rises above or sets beyond the horizon, as expected ($\chi = 90^\circ$ separates daytime and nighttime observations). The daytime TEC is described well by the Klobuchar-like trend $A \cos \chi + B$ [Klobuchar, 1987]. However, near the $\chi = 90^\circ$ value this trend falls off too slowly and the binned TEC appears to be more consistent with the $A \cos^{1/2} \chi + B$ model trend. This is also reflected in the smaller chi-squared parameter for both ITEC and VTEC. The nighttime PFISR TEC observations are affected by the lack of points

with small uncertainties; therefore, the point occurrence in Figure 4a drops off at $\chi > 90^\circ$.

[32] The points in Figure 4a exhibit some scatter for the same value of χ (± 1 TECU), a probable result of considering together many events which occurred under different geophysical conditions. In particular, TEC is known to depend on the solar activity [e.g., Liu and Chen, 2009]. In Figures 4c and 4d this dependence is investigated by plotting the mean SOHO EUV flux for each plot cell. These two panels exhibit a clear color-coding pattern showing that larger (smaller) fluxes correspond to larger (smaller) TEC values during daytime, as expected. A daytime TEC increase with the EUV flux is also evident from the binned values that are, on average, higher at larger fluxes (red points), and from the red fitted trend being higher than the blue trend. However,

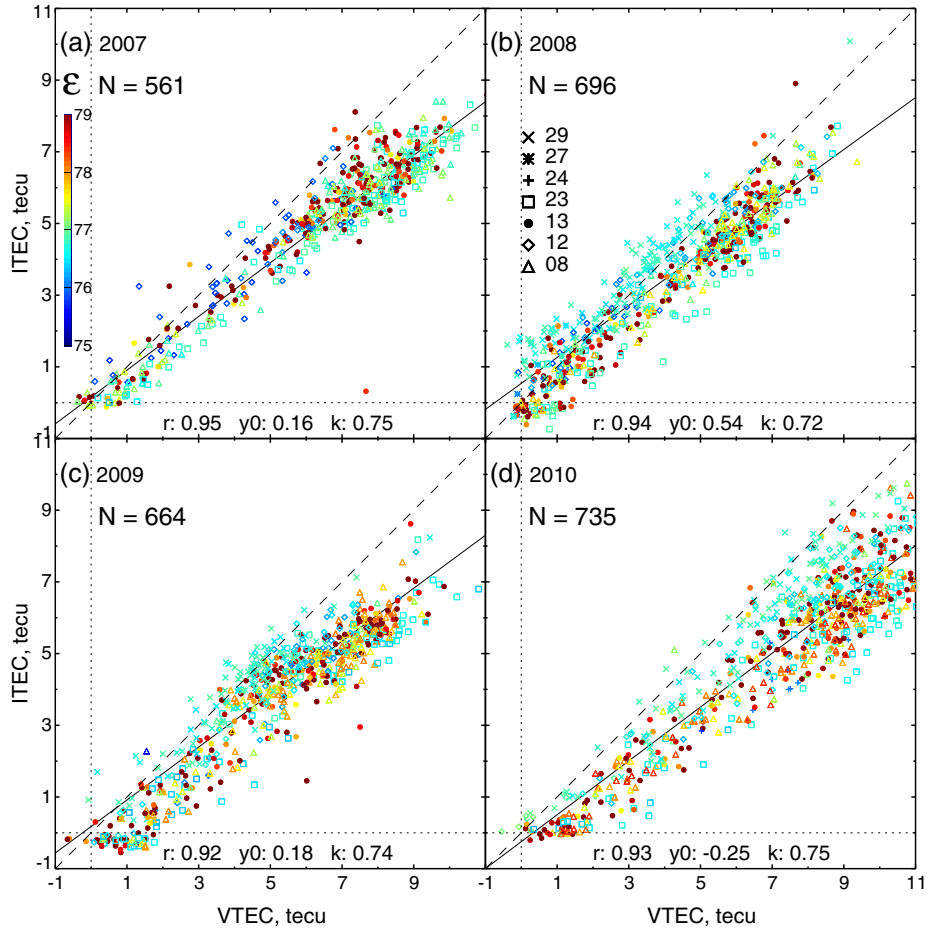


Figure 5. (a–d) Point-by-point comparison of TEC derived from PFISR and GPS measurements in 2007–2010. The points are color coded in GPS satellite elevation angle ϵ and symbol coded in PRN. The coding schemes are shown in Figures 5a and 5b. The total number of points N is also given. The dashed line is the ideal coincidence line, while the solid line is the linear least-squares fit. The linear Pearson correlation coefficient r , intercept y_0 in TECU, and slope k of the linear fit are shown in each panel.

there is still plenty of variation even for the same value of the mean flux. In addition, the EUV flux effect is opposite for nighttime observations; i.e., TEC appears to be smaller for higher fluxes. Both observations suggest that other factors not considered here may be important, e.g., possible changes in EUV or particle spectra.

[33] In general terms, however, TEC appears to behave similarly to the previously documented GPS TEC trends; i.e., it increases with decreasing SZA and increasing solar activity. The standard deviations in the TEC values binned in χ were not overly large, ~ 1 TECU from Figure 4, and this presents an opportunity to examine the behavior of TEC residuals versus SZA and solar flux (Figures 4e and 4f). The TEC difference, on average, decreased with χ and, although the changes were within uncertainty, the decrease in averages was very clear and consistent with that seen in Figure 3 (third row), where $VTEC - ITEC$ also decreased significantly from daytime to nighttime hours. The $ITEC/VTEC$ ratio, on the other hand, was quite stable at $\chi < 90^\circ$ and showed some increase, on average, at $\chi > 90^\circ$. This increase was again consistent with that seen in Figure 3 (bottom row). The difference in the binned TEC was marginally higher at higher fluxes (Figure 4e), and the ratio was marginally

lower (Figure 4f). This result is probably related to a general increase (decrease) in the TEC difference (ratio) from 2007 to 2010 observed in Figure 3.

5. Direct Comparison of TEC Measurements

[34] In this section, the TEC values derived from the PFISR and GPS measurements are compared using very strict criteria for the timing of both measurements and also for their locations in space; i.e., only the best conjunctions are considered, as discussed in section 2. Figures 5a–5d show the results of these comparisons for years 2007–2010. The symbol coding is in PRN (the same as in Figure 2), and color coding is in the elevation angle ϵ . The dashed line is the ideal coincidence line, while the solid line is the best least-squares linear fit. The output parameters of the linear fit are also given.

[35] The correlation coefficients between the two sets of measurements were between 0.92 and 0.95. The slopes were also close to each other, 0.72–0.75, while the intercepts were below 0.6 TECU in magnitude. The ITEC values were mostly below the VTEC values. Some point structuring is evident in the elevation angle (color coding) and, to

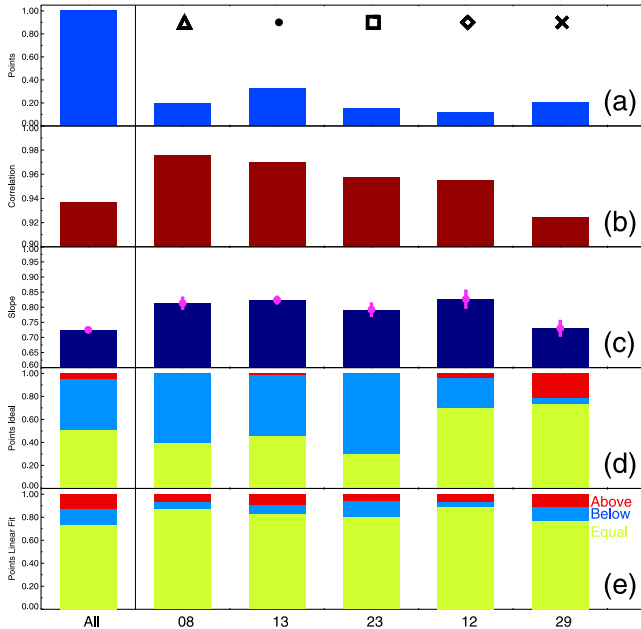


Figure 6. GPS and PFISR comparison results in 2008 for various GPS satellites. PRN is indicated at the bottom, and the corresponding symbol (the same as in Figure 5) is given at the top. The parameters shown are (a) the total number of points as a fraction of the yearly data set, (b) the linear Pearson correlation coefficient, (c) the slope from the linear least-squares fit with uncertainty, (d) the fraction of points that were on (green), above (red), or below (blue) the ideal coincidence line within uncertainty, and (e) the fraction of points on, above, or below the linear fit trend.

a lesser extent, in PRN (symbol coding). The point structuring is most pronounced in 2008, where points at the largest ϵ (red to yellow and some greens) cluster around the linear trend, while other points (mostly crosses and squares) are located farther from this solid line. A significant fraction of measurements, mostly for PRN 29 in 2008, are slightly above the ideal coincidence line, i.e., $\text{ITEC} > \text{VTEC}$, which is somewhat unexpected. This suggests that at least some measurements may still be affected by residual DIB effects and provides one reason why the following analysis considered measurements for individual PRNs separately. In addition, uncertainties in each individual measurement were not shown in Figure 5 to keep the diagram readable, but they were considered explicitly in the following analysis.

[36] Figure 6 shows five selected parameters for all points combined (first column) and for five individual PRNs separately for the 2008 data set. The satellites were sorted in the order of decreasing correlation (Figure 6b). The highest correlations were obtained for PRNs 8 and 13 with the two largest angles ϵ near 77.5° and 79° , respectively. These were also the PRNs closest to PFISR (Figure 1b). The lowest correlation was achieved for satellite 29, with the second lowest angle $\epsilon \approx 76.5^\circ$. From Figure 6c, the slopes of the linear fit were slightly different even with uncertainties considered. This again suggests that DIB effects may have not been completely removed from the GPS data.

[37] The green bars in Figures 6d and 6e represent the fractions of points that were consistent (within uncertainty)

with the dashed ideal coincidence line (Figure 6d) and solid linear fit trend (Figure 6e) in Figure 5b, respectively. The blue (red) bar similarly shows the points that were below (above) these trends. One should stress here that consistency with the ideal coincidence line should not be considered in isolation because systematic differences are expected due to the limited altitude range of PFISR measurements. In other words, it is expected that $\text{ITEC} < \text{VTEC}$ because of the finite topside contribution.

[38] In this context, the linear fit slope k can be used to correct ITEC (to yield $\text{VTEC} \approx k \text{ITEC}$) representing a TEC residual similar to the ratio $r = \text{ITEC}/\text{VTEC}$. Once this correction is determined, it is more instructive to analyze how the point fractions change from Figures 6d to 6e. The fraction of “consistent” points (green bar) increased from $\sim 50\%$ to 75% overall, while for individual satellites the increase was even large, meaning that the linear fit worked well. Most of the “inconsistent” points were below the ideal coincidence line (blue bar), except for satellite 29, as was observed before in Figure 5. With respect to the linear fit, the points above and below were approximately equal in numbers (Figure 6e), which also indicates that the quality of the linear fit was reasonable.

[39] Overall, the direct comparison between closely matched data points demonstrates the importance of considering individual PRNs. Even though all considered measures of agreement (correlation, slope of linear fit, fraction of points consistent with the linear fit) were close to each other, measurable differences were also found. Some of these may be due to unremoved DIBs and some due to spatial effects. The agreement was generally better for higher elevation angles and PRNs whose sub-ionospheric points were closer to PFISR; this is further investigated in the following section.

6. Factors Affecting Agreement Between GPS and ISR

[40] In this section, we analyze the residual TEC expressed as a ratio $r = \text{ITEC}/\text{VTEC}$. The basis for this analysis is that r will be close to the slope of the linear fit k for points that agree well, with significantly different values for points away from the linear fit. Figure 7 shows the ratio versus selected parameters of interest for measurements in 2008. Only points with small absolute ($< 2 \text{TECU}$) and relative ($< 50\%$) uncertainties in ITEC and VTEC were considered. The parameters considered were the following: (a) SZA χ , (b) UT, (c) GPS elevation angle ϵ , and (d) distance from GPS receiver station FAIR. The color coding is in angle χ , while symbol coding is again in PRN. The black line is the median ratio for each bin in the respective parameter. The gray-shaded area represents the limits of slopes from Figure 6c.

[41] Figure 7a shows that for daytime observations $\chi < 80^\circ$ many points fell within the gray-shaded area, and the binned median of TEC ratio was consistent with the slope of the linear fit. In Figure 7b, the same feature is also present between 14:00 and 06:00 UT, although in this panel, points for PRN 29 “contaminate” observations between 00:00 and 08:00 UT. This satellite covers angles $\chi = 80^\circ\text{--}95^\circ$ (Figure 7a), and these conjunctions correspond to observations near the solar terminator despite their “early” UT

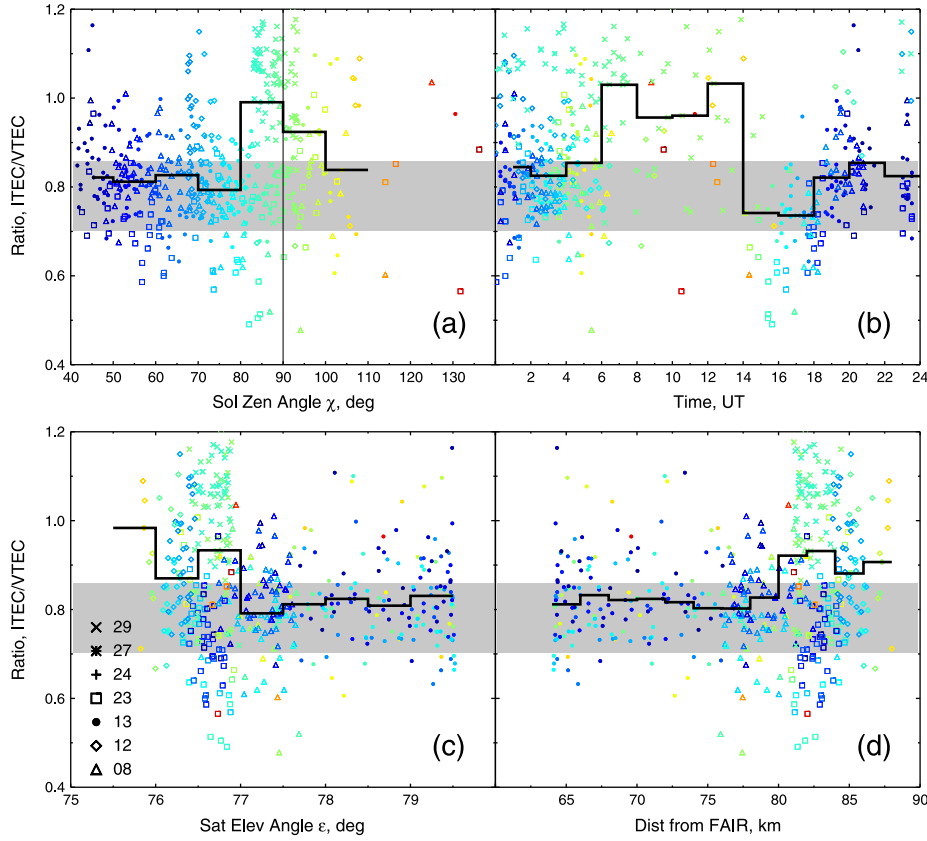


Figure 7. The ratio $ITEC/VTEC$ versus four selected parameters (a)-(d) for conjunctions in 2008. The color coding is in the solar zenith angle χ as represented by Figure 7a, while symbol coding is in PRN. The shaded area represents the limits of the slope values from Figure 6c. The black line shows the median ratio for the binned data.

(Figure 2c). In the region corresponding to the solar terminator and nightside, the ratios were generally higher with most points and median above the gray-shaded area (Figures 7a and 7b). This result is consistent with that seen from the averages presented in Figures 3 and 4, where the ratio of average $ITEC$ to $VTEC$ was also higher on the nightside. This implies that the topside contribution to TEC is smaller in this region.

[42] Figures 7c and 7d show that most points and the binned median were within the gray-shaded area for angles $\epsilon > 77^\circ$ and distances < 80 km. This implies that the consistency between individual ratios and slope values is higher for observations that were close in elevation and distance. This is consistent with the notion that spatial differences affect the agreement between observations. At $\epsilon < 77^\circ$ and distances > 80 km, the points spread was much higher and the median was above the gray-shaded area. These conjunctions were mostly with PRNs 12, 23, and 29, and these data sets had the lowest correlations (Figure 6b). This indicates that other effects such as residual DIBs may have contributed to poorer agreement for these observations.

[43] Overall, the analysis of individual conjunctions and the TEC residuals derived from them yielded similar results to those using TEC averages for specific time and SZA intervals (sections 3 and 4). In particular, we found higher and less consistent $ITEC/VTEC$ ratios near the solar terminator and on the nightside. In addition, we demonstrated the

importance of considering specific conjunctions described in terms of PRN, elevation angle, and distance between measurement locations.

7. Discussion

[44] This study represents a first statistical analysis and comparison of TEC estimates derived from two radio techniques used to observe the plasma content in the near-Earth space dominated by the F region ionosphere. We analyzed the GPS- and ISR-derived TEC estimates in the auroral region, as well as their residuals that represent the topside contribution to TEC . By using an extensive data set collected over 4 years and strictly matching the measurements in time and in space, this study investigated quantitatively both the average trends in TEC residuals and the specific factors that control consistency with these trends. Below we discuss both instrumental and geophysical effects that can potentially contribute to the observed differences in the GPS- and ISR-derived TEC estimates.

7.1. Instrumental Effects and Limitations

[45] PFISR covers a substantial portion of the ionosphere with a maximum altitude of 663 km and a good range resolution of 72 km (or 36 km for half-pulse-width products). This allows us to derive $ITEC$ estimates of reasonable quality; for example, in our 2008 observations $\sim 74\%$ (57%) points had

uncertainties below 2 TECU (50%). In addition, PFISR routinely provides observations with distances 10–80 km from the GPS sub-ionospheric points or 65–90 km from FAIR (Figures 1b and 7d), which minimizes spatial differences.

[46] The PFISR electron densities are obtained from the returned power calibrated using plasma line observations, which on occasions resulted in spurious density values such as the high values on selected days listed in section 2 or small negative values that were present in Figure 5. The former were excluded manually, while the latter were kept within the data set, since these ITEC values were close to zero and generally within the uncertainty of these estimates. These small negative values, however, were excluded from data sets with large number of observations when relative uncertainties in ITEC were limited to <50%, e.g., no such points were present in Figure 4a.

[47] The GPS TEC estimates were obtained from FAIR, one of the few IGS Reference Frame stations in the auroral region. The data quality was very high throughout the period of interest, with very few cycle slips which were found and corrected by the algorithm. The number of negative VTEC values was also very small (e.g., Figure 5), which indicates that a DIB estimate for FAIR from the IGS (JPL) TEC maps was also reasonably good. On the other hand, measurable differences were found between conjunctions with specific PRNs (Figure 6). In particular, the data set for PRN 29 was the only one that showed more points above the ideal coincidence line than points below it; its correlation was also the lowest of all PRNs (0.92). This suggested that some small residual DIB effects may have been present in GPS VTEC estimates, particular for those PRNs that yielded more VTEC < ITEC estimates.

7.2. TEC Contribution From the Topside Ionosphere

[48] One can argue that the greatest source of discrepancies between ITEC and VTEC measurements is the topside plasma content that cannot be measured with PFISR. While this presents a challenge for cross-calibration efforts, it also provides an opportunity for investigating the topside contribution to TEC through examination of TEC residuals as described in section 1. In the past, similar efforts have focused on midlatitude and low-latitude comparisons between GPS and ionosonde observations and the associated plasmaspheric contribution [Belehaki *et al.*, 2003; Meza *et al.*, 2008], while most of our experimental knowledge about topside dynamics at auroral latitudes comes from low-Earth-orbit satellites observing either at or below the orbital altitude.

[49] In our observations, the TEC residuals referred to plasma content at altitudes above 660 km. The diurnal and seasonal variations in plasma content were found to be broadly consistent with those in the lower ionosphere (Figure 3), i.e., higher on the dayside and lower on the nightside. One exception, however, was that a maximum was observed in the morning rather than near magnetic noon. This behavior was different from that found at midlatitudes where two maxima are observed, a stronger evening maximum and a weaker morning maximum [Belehaki *et al.*, 2003]. The topside and plasmaspheric plasma content may be influenced by the upward diffusion from the ionosphere during the day and the downward plasma flow into the ionosphere at night. The exact shape

of the diurnal variation is difficult to predict without information about the relative strength of these processes versus time. However, the present observations indicate that the maximum in the topside plasma content occurs earlier than its counterparts in either the *F* region ionosphere or the plasmasphere.

[50] The topside contribution to TEC was also investigated for various solar conditions as described by SZA χ and solar EUV flux (Figure 4). In absolute terms or when expressed as a simple difference VTEC – ITEC, this contribution decreased with χ and increased with the EUV flux on the dayside (Figure 4e). The ratio $r = \text{ITEC}/\text{VTEC}$ was quite stable during the day and marginally larger at night, implying a decrease in the topside contribution at night, when expressed as a fractional difference $1 - r$. The topside contribution increase with solar cycle and hence with solar activity was also observed in Figure 3. This result implies that the *F* region and the topside ionosphere behave in a largely similar way with respect to the solar activity. Since the *F2* layer tends to persist into the night, while the *F1* layer disappears, one could perhaps expect a stronger fractional difference $1 - r$ at night. Our observations show that this does not happen, and instead the behavior of the topside ionosphere largely mimics that of the dominant *F2* layer.

[51] The topside contribution was estimated using various methods, from examination of ITEC and VTEC averages for particular time and SZA intervals to linear fits to TEC estimates for closely matched conjunctions. All methods produced very similar results. Thus, typical ratios were 0.80 ± 0.20 from Figure 4f, 0.725 ± 0.009 from Figure 6c, and 0.70–0.85 from Figure 7. The most precise estimates were obtained from linear fits to yearly data sets of GPS/PFISR conjunctions (Figure 5); from these the topside contribution was $\sim 1/4$ of TEC. This is lower than a factor of $\sim 1/2$ obtained by *Lilensten and Cander* [2003] for their $\text{ITEC}_{498}/\text{VTEC}$ estimates, which is expected given an ~ 160 km difference in maximum ISR altitudes. Coincidentally, this result also implies that the same amount ($1/4$) falls between 498 and 660 km as between 660 and 20,200 km.

7.3. Other Factors Affecting TEC Comparisons

[52] The finite topside contribution to TEC provides a source of systematic discrepancies between GPS and PFISR as discussed above. This question is addressed here: What are other factors that can affect the agreement between them?

[53] As discussed in section 7.1, one such factor may be small residual DIB effects that are not completely removed from GPS data. A general conclusion derived from analysis presented in section 5 was that various measures of agreement showed some differences between conjunctions with specific PRNs (Figures 5 and 6). It was also found that two other factors, GPS elevation angle and distance between measurement locations, appeared to influence the agreement (section 6). The agreement was poorer for smaller elevations and larger distances, as indicated by an increase in the point scatter and the binned median being higher than the slope limits (Figures 7c and 7d). These two factors are somewhat related because elevation angles were generally smaller for larger distances due to GPS coverage biases (Figure 1b). By the same token, one cannot completely rule

out a possibility that DIB effects have also contributed to the poorer agreement at smaller elevations and larger distances. The fact that at least three different PRNs observed poorer agreement suggests that the two spatial effects were more important.

[54] The higher point scatter and binned median near the solar terminator $\chi = 90^\circ$ can be also interpreted in terms of spatial gradients and/or residual DIB effects, since most of these observations refer to a particular PRN 29 (Figures 7a and 7b). The fact that a higher ratio of nighttime averages was also observed in other analyses that included other PRNs (Figures 3 and 4) suggests that spatial effects were stronger.

8. Summary and Conclusions

[55] Statistical analysis of an extensive data set of TEC estimates derived from the GPS and PFISR measurements in the auroral region showed the following:

[56] 1. The GPS- and PFISR-derived TEC estimates exhibited very similar and distinct diurnal, seasonal, and solar cycle dependencies. TEC is strongly controlled by the solar zenith angle and activity conditions. The average daytime TEC dependence on the solar zenith angle χ is described well by a Klobuchar-like model involving cosine trend with constant offset; a trend involving $\cos^{1/2}\chi$ results in a slightly better fit.

[57] 2. The topside ionosphere above 660 km contributes $\sim 1/4$ of TEC at auroral latitudes, with larger average contribution during the day and under high solar activity conditions. The TEC residuals exhibit a different diurnal variation from that found at midlatitudes, possibly because the plasmasphere is not observed at these latitudes. The topside contribution estimates based on close conjunctions were most consistent during daytime hours, while observations near the solar terminator and during the night had larger uncertainties and higher variability.

[58] 3. The PFISR- and GPS-derived TEC estimates closely matched in space and in time had typical correlations of ~ 0.93 and ratios of ~ 0.75 . The agreement was very consistent between yearly data sets, although some differences were found between conjunctions with specific GPS satellites. The largest discrepancies were observed at solar zenith angles near to and greater than 90° , at the smallest GPS satellite elevation angles, and for the largest distances between measurement locations. This is attributed to a combined effect of spatial differences and unremoved instrumental biases.

[59] **Acknowledgments.** PFISR is operated by SRI International under NSF Cooperative Agreement AGS-1133009. Additional support for this research was provided by NSF grant AGS-1243476. The GPS data were obtained using the International Global Navigation Satellite Systems Service. The SOHO/SEM EUV data were downloaded from the website http://www.usc.edu/dept/space_science/. The authors are grateful to B. J. Watkins for useful discussions.

References

- Baker, K. B., and S. Wing (1989), A new magnetic coordinate system for conjugate studies at high latitudes, *J. Geophys. Res.*, *94*, 9139–9143.
- Belehaki, A., N. Jakowski, and B. W. Reinisch (2003), Comparison of ionospheric ionization measurements over Athens using ground ionosonde and GPS-derived TEC values, *Radio Sci.*, *38*, 1105, doi:10.1029/2003RS002868.
- Foster, J. C., et al. (2005), Multiradar observations of the polar tongue of ionization, *J. Geophys. Res.*, *110*, A09S31, doi:10.1029/2004JA010928.
- Heinselman, C. J., and M. J. Nicolls (2008), A Bayesian approach to electric field and *E*-region neutral wind estimation with the Poker Flat Advanced Modular Incoherent Scatter Radar, *Radio Sci.*, *43*, RS5013, doi:10.1029/2007RS003805.
- Huang, C.-S., J. C. Foster, L. P. Goncharenko, P. J. Erickson, W. Rideout, and A. J. Coster (2005), A strong positive phase of ionospheric storms observed by the millstone hill incoherent scatter radar and global GPS network, *J. Geophys. Res.*, *110*, A06303, doi:10.1029/2004JA010865.
- Klobuchar, J. A. (1987), Ionospheric time-delay algorithm for single-frequency GPS users, *IEEE Trans Aerosp Electron Syst.*, *23*, 325–331.
- Komjathy, A., L. Sparks, B. D. Wilson, and A. J. Mannucci (2005), Automated daily processing of more than 1000 ground-based GPS receivers for studying intense ionospheric storms, *Radio Sci.*, *40*, RS6006, doi:10.1029/2005RS003279.
- Lilinsten, J., and L. R. Cander (2003), Calibration of the TEC derived from GPS measurements and from ionospheric models using the EISCAT radar, *J. Atmos. Sol. Terr. Phys.*, *65*, 833–842.
- Lilinsten, J., L. R. Cander, M. T. Rietveld, P. S. Cannon, and M. Barthélémey (2005), Comparison of EISCAT and ionosonde electron densities: Application to a ground-based ionospheric segment of a space weather programme, *Ann. Geophysicae*, *23*, 183–189.
- Liu, L., and Y. Chen (2009), Statistical analysis of solar activity variations of total electron content derived at Jet Propulsion Laboratory from GPS observations, *J. Geophys. Res.*, *114*, A10311, doi:10.1029/2009JA014533.
- Lunt, N., L. Kersley, G. J. Bishop, and A. J. Mazzella (1999), The contribution of the protonosphere to GPS total electron content: Experimental measurements, *J. Atmos. Sol. Terr. Phys.*, *34*, 1273–1280.
- Makela, J. J., S. A. González, B. MacPherson, X. Pi, M. C. Kelley, and P. J. Sultan (2000), Intercomparisons of total electron content measurements using the Arecibo incoherent scatter radar and GPS, *Geophys. Res. Lett.*, *27*, 2841–2844, doi:10.1029/2000GL000023.
- Mannucci, A. J., B. D. Wilson, D. N. Yuan, C. H. Ho, Lindqwister, U. J., and T. F. Runge (1998), A global mapping technique for GPS-derived ionospheric total electron content measurements, *Radio Sci.*, *33*, 565–582.
- Mendillo, M. (2006), Storms in the ionosphere: Patterns and processes for total electron content, *Rev. Geophys.*, *44*, RG4001, doi:10.1029/2005RG000193.
- Mendillo, M., and J. A. Klobuchar (2006), Total electron content: Synthesis of past storm studies and needed future work, *Radio Sci.*, *41*, RS5S02, doi:10.1029/2005RS003394.
- Meza, A., C. Brunini, A. E. Gularte Scarone, and M. Mosert (2008), Analysis of a topside ionospheric model using GPS and ionosonde observables, *Adv. Space Res.*, *42*, 712–719.
- Nicolls, M. J., M. C. Kelley, A. J. Coster, S. A. González, and J. J. Makela (2004), Imaging the structure of a large-scale TID using ISR and TEC data, *Geophys. Res. Lett.*, *31*, L09812, doi:10.1029/2004GL019797.
- Rietveld, M. T., P. N. Collis, A. P. Vaneyken, and U. P. Lovhaug (1996), Coherent echoes during EISCAT UHF Common Programmes, *J. Atmos. Terr. Phys.*, *58*, 161–174.
- Sedgemore-Schulthess, F., and J.-P. St. Maurice (2001), Naturally enhanced ion-acoustic spectra and their interpretation, *Surv. Geophys.*, *22*, 55–92.
- Sojka, J. J., M. J. Nicolls, C. J. Heinselman, and J. D. Kelly (2009), The PFISR IPY observations of ionospheric climate and weather, *J. Atmos. Sol. Terr. Phys.*, *71*, 771–785.
- Yizengaw, E., M. B. Moldwin, D. Galvan, B. A. Iijima, A. Komjathy, and A. J. Mannucci (2008), Global plasmaspheric TEC and its relative contribution to GPS TEC, *J. Atmos. Sol. Terr. Phys.*, *70*, 1541–1548.